A nickel based superalloy reinforced by both Ni_3Al and Ni_3V ordered-fcc precipitates

Alexander J Knowles[a,b,*], Lucy Reynolds[a], Vassili A Vorontsov[a], David Dye[a]

[a]*Department of Materials, Imperial College, South Kensington, London SW7 2AZ, UK*
[b]*School of Metallurgy and Materials, University of Birmingham, Birmingham, B15 2TT, UK*

Abstract

A nickel based superalloy has been designed where the fcc γ Ni matrix is reinforced by two different ordered-fcc intermetallic compounds, γ' $L1_2$ Ni_3Al and γ'' $D0_{22}$ Ni_3V. Primary ageing at $900 - 1000\,°C$ precipitated spherical $L1_2$ Ni_3Al, whose volume fraction and size were controlled by altering the ageing temperature and time. Secondary ageing at $700\,°C$ for $1 - 1000\,h$ precipitated $D0_{22}$ Ni_3V laths. The duplex precipitation increased hardness by up to 85 HV, with ~ 500 MPa compressive proof strength maintained at $800\,°C$. Electron microscopy studied the Ni_3Al precipitation and confirmed the form of the secondary Ni_3V precipitates and their long term stability.

Keywords: Superalloy, Precipitation, Intermetallics, Microstructure, Mechanical properties

Nickel based superalloys are widely used due to their combination of strength, creep, toughness, environmental resistance and microstructural stability in the $650 - 1200°C$ interval [1, 2]. Such alloys exploit the two-phase field that exists within the Ni-Al binary system to produce microstructures comprising a
5   γ face-centred cubic (fcc) A1 (*Strukturbericht designation*) matrix, Figure 1a, reinforced with γ' $L1_2$ Ni_3Al ordered-fcc intermetallic precipitates, Figure 1b. A variety of additional phases are used in multicomponent (~ 10) commercial superalloys, including other intermetallics as well as carbides and borides. However, there is an additional ordered-fcc $D0_{22}$ γ'' phase, Figure 1c, that can be
10   exploited in superalloys, *e.g.* Inconel 718 [3], which is also being explored in other alloy systems [4, 5, 6]. Unfortunately, the $D0_{22}$ Ni_3Nb phase in Inconel 718 is metastable [7, 8] decomposing into the δ Ni_3Nb $D0_a$ orthorhombic $Pmmn$ phase [9, 10]. The Ni_3X type intermetallics adopt a number of stable crystal structures as the X element is changed due to differing formation energies. For
15   Ni_3X intermetallics with X = Nb, Ta, Mo the stable structure is $D0_a$, while for X = Ti the $D0_{24}$ structure is adopted, and with X = Al and Si the traditional γ'

L1$_2$ structure is adopted [11]. The only stable D0$_{22}$ Ni$_3$X type intermetallic is Ni$_3$V [11], and notably this has not been exploited in practical alloys. The D0$_{22}$ crystal structure is of particular interest as, unlike the D0$_a$ and D0$_{24}$ structures, it is an fcc superlattice structure, being ordered across two fcc unit cells with a 3:1 A to B site ratio (Figure 1c). Because of its distinct crystal structure, composition, lattice parameter and so misfit, D0$_{22}$ Ni$_3$V may exhibit a different morphology to L1$_2$ Ni$_3$Al as well as different coarsening kinetics and strengthening effects [12, 13, 14]. D0$_{22}$ Ni$_3$V has lattice parameters of a = 3.543 Å, c = 7.221 Å[15], compared to those for metastable D0$_{22}$ Ni$_3$Nb of a = 3.62 Å, c = 7.41 Å [7].

In this work the D0$_{22}$ Ni$_3$V phase is explored. Purely on density grounds it may be of interest as the density of its unit cell is 8% lower than pure Ni, compared to 2% higher for D0$_{22}$ Ni$_3$Nb and 18% lower for L1$_2$ Ni$_3$Al. The Ni$_3$V phase offers some advantages over Ni$_3$Nb as it is thermodynamically stable and has a different lattice misfit, δ. Given $\delta = 2(a_{\gamma'} - a_\gamma)/(\gamma' + a_\gamma)$ and $a_\gamma = 3.51$ Å, δa$_\gamma$-a$_{Ni_3V} \sim 0.9\%$, and δa$_\gamma$-c$_{Ni_3V} \sim 2.8\%$, in contrast to δa$_\gamma$-a$_{Ni_3Nb} \sim 3.1\%$, and δa$_\gamma$-c$_{Ni_3Nb} \sim 5.4\%$, taking the lattice parameters given earlier for Ni$_3$V [15] and Ni$_3$Nb [7]. Further, it is possible to have controlled precipitation of L1$_2$ Ni$_3$Al with optimised volume fraction and size before producing D0$_{22}$ Ni$_3$V at a lower temperature. This is because in the Ni-Al-V ternary system the A1 Ni phase exists in equilibrium with L1$_2$ Ni$_3$Al at 1000 °C, Figure 1d. However, when the temperature is lowered to 700 °C a three phase field exists between A1 Ni, L1$_2$ Ni$_3$Al and D0$_{22}$ Ni$_3$V, Figure 1e [16]. This enables the L1$_2$ Ni$_3$Al population to be established and controlled prior to formation of D0$_{22}$ Ni$_3$V, Figure 1f. A two-step heat treatment was designed to investigate the potential to form hierarchical structures of D0$_{22}$ Ni$_3$V within L1$_2$ Ni$_3$Al precipitates, as is possible in B2 and L2$_1$ ordered-bcc precipitates [17] and L1$_2$ Ni$_3$Al with A1 Ni precipitates [18, 19, 20].

A 300 g ingot of the Ni-14.9%V-5.2%Al (at.%) alloy was prepared by arc melting of pure (> 99.9%) elements under Ar, which was used to characterise the stable phases at particular temperatures. Sections of the alloy were heat treated under protected atmosphere using evacuated quartz ampoules backfilled with argon.

The alloy was solution heat treated at 1240 °C for 24 h and water quenched. Primary ageing heat treatments were made at 1000 °C and 900 °C for 16 h to 500 h and water quenched. Secondary ageing heat treatments were made at 700 °C for 10 h to 1000 h and water quenched. Scanning electron microcopy (SEM) was performed on a Zeiss Sigma 300 operated at 5 or 10kV for imaging and JEOL 6400 operated at 20 kV for energy-dispersive X-ray spectrometry (EDX). The bulk composition of the alloy evaluated by a 200×400 μm EDX area measurement, was (79.0 ± 0.2)Ni – (15.6 ± 0.1)V – (5.4 ± 0.2)Al (at.%), which was considered sufficiently close to the target composition to meet the needs of the study.

The density, determined by the Archimedes method, was 8.27 g cm^{-3}. X-ray diffraction was performed to determine the phases present in the alloy using Cu$_{K\alpha}$ radiation on spun flat samples ~ 8 mm in diameter. Transmission electron

microscopy (TEM) and scanning TEM (STEM) were performed using a JEOL 2100F microscope. TEM foils were prepared by mechanical thinning to $150\,\mu m$ followed by eletropolishing using 10 vol.% perchloric acid in methanol at $-8\,°C$ and $18\,V$. Hardness indents using a $10\,kg$ load held for $10\,s$ were made with the average of five measurements reported. High temperature compression tests to determine the variation in 0.2% proof strength with temperature were performed on sub-sized $2\,mm$ cube samples that were tested at a strain rate of $10^{-3}\,s^{-1}$ under vacuum within a modified $5\,kN$ Zwick load frame up to $800\,°C$ [21].

The stable phases in the alloy were evaluated at a number of different times and temperatures. Homogenisation at $1240\,°C$ for $24\,h$ was found to be successful at removing casting-induced microsegregation and resulted in a grain size of $\sim 300\,\mu m$ (determined by the linear intercept method), see Figure 2c. Following ageing at $1000\,°C$ for $16\,h$, an area fraction of 15% spherical precipitates was attained with $\sim 340\,nm$ diameter, Figure 2d. Further ageing to $200\,h$ at $1000\,°C$ resulted in these precipitates coarsening to $\sim 680\,nm$ in size. In contrast, ageing at $900\,°C$ for $200\,h$ resulted in a greater area fraction of 40% precipitates of $\sim 230\,nm$ size (Figure 2e), which coarsened to $\sim 350\,nm$ after $500\,h$ total ageing time. Secondary ageing at $700\,°C$ was found to give a pronounced change in the microstructure of the alloy with the matrix phase found to contain a second form of precipitates produced with a lath morphology. After $100\,h$ these exhibited a thickness of $14 \pm 4\,nm$ and a spacing of $25 \pm 8\,nm$, Figure 2f. Further ageing to $1000\,h$ coarsened the lath precipitates to a thickness of $21 \pm 4\,nm$ and a spacing of $42 \pm 15\,nm$, Figure 2g.

X-ray diffraction was used to study the phases present in each heat treated condition, shown in Figure 2a. In the homogenised condition reflections consistent with single phase A1 fcc were observed. On primary ageing at $900\,°C$, as well as A1 reflections, additional reflections consistent with an ordered-fcc $L1_2$ phase were found indicating that the second phase present in SEM (Figure 2e) was $L1_2$ Ni_3Al. Secondary ageing at $700\,°C$ resulted in A1 and $L1_2$ phase reflections as well as additional reflections suggestive of a phase with the alternative ordered-fcc $D0_{22}$ structure, which were suspected to originate from the lath precipitates observed by SEM (Figure 2f and g). However, the $D0_{22}$ peaks were weak owing to the structure factor. Further study of the precipitates and the elemental segregation between phases were made by TEM and STEM as the size of the phases were below the resolution limit of SEM-EDX.

Vickers microhardness results from the alloy in each heat treated condition are shown in Figure 3a with a $700\,°C$ ageing curve following the $900\,°C$ for $200\,h$ primary age. This is plotted alongside alternative primary ages of $900\,°C$ $500\,h$ and $1000\,°C$ $200\,h$ before and after ageing at $700\,°C$ $100\,h$. Of the explored primary ageing treatments, $900\,°C$ $200\,h$ was found to give the greatest hardness increase of ~ 25 HV when compared to the homogenised condition and so was selected for further secondary ageing. All primary age variants exhibited a further ageing response of ~ 60 HV on secondary ageing that was attributed to the laths observed by SEM (Figure 2f and g). Long duration ageing for $1000\,h$ found only a small hardness loss when compared to the $100\,h$ peak hardness. Shorter ageing times are desirable from a commercial viewpoint, which could

3

be met either by using the alloy in the underaged condition, or using higher secondary ageing temperature where peak hardness would be anticipated after shorter times. Further work is needed to evaluate this and the overall balance of properties achieved.

High temperature compression tests were performed on the alloy after ageing at $900\,^{\circ}$C for $200\,$h and then $700\,^{\circ}$C for $100\,$h in order to evaluate its proof strength, Figure 3b. For comparison, Inconel 718 [3] superalloy and Haynes 230 [22] solid solution alloy are used. Whilst the 0.2% proof stress ($\sigma_{y,0.2}$) of 695 MPa found at room temperature was significantly lower than IN718 [3], the $800\,^{\circ}$C $\sigma_{y,0.2} \sim 500$ MPa was comparable, and the alloy out-performed H230 [22] at all temperatures evaluated. These findings for the simple ternary alloy are promising when compared to complex commercialised alloys with their many additions and optimisation iterations. Superalloys are typically exposed to oxidising conditions at high temperature and so it is important for their oxidation resistance to be evaluated. Thermogravimetric analysis (TGA) of the alloy, primary aged at $900\,^{\circ}$C for $200\,$h and secondary aged at $700\,^{\circ}$C for $100\,$h, was performed at $700\,^{\circ}$C for $24\,$h in air found parabolic oxidation kinetics, with a power law ($y = x^n$) exponent of n=0.52, see Supplementary Figure 2. However, this was markedly faster than that reported for IN718 [23] after $24\,$h, which was attributed to the lower Al and Cr contents in the simple ternary alloy.

Scanning transmission electron microscopy (STEM) was performed to study the secondary precipitates in greater detail on a coarsened sample that was primary aged at $900\,^{\circ}$C for $200\,$h and then long duration secondary aged at $700\,^{\circ}$C for $1000\,$h. TEM and STEM analysis was also performed after $100\,$h, see supplementary information. In this condition SADPs were obtained from purely the spherical L1$_2$ Ni$_3$Al precipitates (Figure 4a), as well as from both spherical and lath precipitates (Figure 4b). STEM annular dark field (ADF) imaging was then used and by carefully positioning the objective aperture it was possible to not only highlight the L1$_2$ precipitates (Figure 4c) but also to separate and image using solely the D0$_{22}$ superlattice reflections (Figure 4d). The latter were found to correspond to the lath precipitates, confirming that they were D0$_{22}$ structured. STEM-EDX mapping of the sample (Figure 4e-h) again found Al segregation to the L1$_2$ precipitates consistent with Ni$_3$Al. However, it was also found that the coarsened laths were rich in V consistent with them being Ni$_3$V, where the equal aluminium concentration between A1 Ni and D0$_{22}$ Ni$_3$V matches the phase diagram (Figure 1b). Whilst richer in V, it was found that a significant quantity of V was dissolved within the L1$_2$ Ni$_3$Al. This is in agreement with the marked ternary solubility for V in Ni$_3$Al within the Ni-Al-V ternary phase diagram (Figure 1a and b).

It was suspected that the solubility for V within L1$_2$ Ni$_3$Al may decrease with temperature in a similar manner to that for hierarchical structured ferritic superalloys. In these alloys the Fe rich A2 matrix contains $60 - 200\,$nm B2 NiAl precipitates from within which $15 - 20\,$nm L2$_1$ precipitates nucleate and grow within the B2 precipitates [17]. This is similar to the precipitation of A1 Ni from within L1$_2$ Ni$_3$Al [18, 19, 20] owing to the decreased solubility for Ni within Ni$_3$Al with temperature. If the solubility for V within Ni$_3$Al changed

4

155 with temperature this would enable the precipitation of $D0_{22}$ Ni_3V from within $L1_2$ Ni_3Al. However, no precipitation within the $L1_2$ Ni_3Al was observed, with the $D0_{22}$ Ni_3V only found within the A1 Ni matrix instead. This indicated that there is minimal change in V solubility within $L1_2$ Ni_3Al from $900\,^\circ$C to $700\,^\circ$C.

In summary, the following conclusions can be drawn.

160 (1) A new nickel based superalloy has been designed and produced that comprises two ordered-fcc precipitates, γ' $L1_2$ and γ'' $D0_{22}$. Such precipitation has been demonstrated for Ni_3Nb in Inconel 718 and other alloys, however, Ni_3Nb is metastable in the $D0_{22}$ structure. In contrast, the stable $D0_{22}$ structured Ni_3V intermetallic observed here has not been explored as a superalloy reinforcing
165 phase.

(2) A peak primary age of $900\,^\circ$C for $200\,$h was determined where 40% area fraction of $\sim 230\,$nm spherical γ' $L1_2$ Ni_3Al precipitates were produced, giving 25 HV hardening. No $D0_{22}$ precipitated at this temperature allowing the γ' formation to be controlled and optimised.

170 (3) Secondary ageing at $700\,^\circ$C for $100\,$h formed fine laths with a thickness of $14 \pm 4\,$nm and a spacing of $25 \pm 8\,$nm, which gave nearly 60 HV of additional hardness. These lath precipitates were determined by TEM to be $D0_{22}$ Ni_3V with chemical segregation consistent with the Ni-Al-V phase diagram. No formation of $D0_{22}$ Ni_3V within the previously formed $L1_2$ Ni_3Al precipitates was
175 observed, indicating that the solubility for V within $L1_2$ Ni_3Al does not change markedly from 900 to $700\,^\circ$C.

[1] M.J. Donachie and S.J. Donachie, Superalloys: A Technical Guide, ASM Int., 2nd ed., 2002.

185 [2] R. Reed, The superalloys: fundamentals and applications, CUP, 2006.

[3] Special Metals, Inconel® alloy 718 datasheet SMC-045 (2007) 1-28.

[4] P.M. Mignanelli, N.G. Jones, E.J. Pickering, O.M.D.M. Messe, C.M.F. Rae, M.C. Hardie, and H.J. Stone, Scripta Mater. 136 (2017) 136-140.

[5] X. Gao, R. Hu, and G. Luo, Scripta Mater. 134 (2017), 15-19.

190 [6] I.J. Moore, M.G. Burke, and E.J. Palmiere, Acta Mater. 119 (2016) 157-166.

[7] A. Kaufman, N.J. Hoffmann, and H. Lipson, Scripta Metal. 3 (1969) 715-720.

[8] Y. Du, Y. A. Chang, W. Gong, B. Huang, H. Xu, Z. Jin, F. Zhang, and S.L. Chen, Intermetallics 11 (2003) 995-1013.

[9] D. Srinivasan, Mat. Sci. Eng. A 364 (2004) 27-34.

5

[195] [10] R. Krakow, D.N. Johnstone, A.S. Eggeman, D. Hünert, M.C. Hardy, C.M.F. Rae, and P.A. Midgley, Acta Mater. 130 (2017) 271-280.

[11] H. Sugimura, Y. Kaneno, and T. Takasugi, Materials Trans. 52 (2011) 663-671.

[12] J.M. Oblak, D.F. Paulonis, and D.S. Duvall, Metallurgical Trans. 5 (1974) 143-153.

[200] [13] D.C. Lv, D. McAllister, M.J. Mills, and Y. Wang, Acta Mater. 118 (2016) 350-361.

[14] Y. Zhao, L. Qi, Y. Jin, K. Wang, J. Tian, and P. Han, J. Alloys and Compounds 647 (2015) 1104-1110.

[15] J. Mass, G. Bastin, F. Loo, and R. Metselaar, Zeitschrift für Metallkunde 74 (1983) 294-299.

[205] [16] H. Zapolsky, C. Pareige, L. Marteau, and D. Blavette, Calphad 25 (2001) 125-134.

[17] C. H. Liebscher, V.R. Radmilović, U. Dahmen, and N. Q. Vo, Acta Mater. 92 (2015) 220-232.

[18] A. J. Ardell and M. Pozuelo, Intermetallics 88 (2017) 81-90.

[19] Y. Ma and A. J. Ardell, Acta Mater. 55 (2007) 4419-4427.

[210] [20] W.H. Tian, T. Sano, and M. Nemoto, Scripta Metal. 20 (1986) 1-4.

[21] T.P. Chapman, K.M. Kareh, M. Knop, T. Connolley, P.D. Lee, M.A. Azeem, D. Rugg, T.C. Lindley, and D. Dye, Acta Mater. 99 (2015) 49-62.

[22] Haynes International, Haynes® 230® alloy datasheet H-3000M (2018) 1-28.

[23] G.A. Greene and C.C. Finfrock, Oxidation of metals 55 (2001) 505-521.

6

Supplementary Information

Supplementary Figure 1 shows scanning transmission electron microscopy (STEM) performed on the alloy after primary ageing at $900\,^{\circ}$C for $200\,$h and secondary ageing at $700\,^{\circ}$C for $100\,$h, from which high-angle annular dark-field (HAADF) imaging revealed both the spherical $L1_2$ precipitates as well as higher resolution imaging of the $D0_{22}$ lath precipitates, compared to SEM. STEM-EDX mapping for Ni, V and Al identified that the spherical precipitates were rich in Al and Ni consistent with them being Ni_3Al. The SADP in Supplementary Figure 1e taken using a $\sim 200\,$nm aperture down the [100] zone axis showed strong $A1$ parent reflections, with weaker $L1_2$ superlattice reflections (blue), as well as $D0_{22}$ superlattice reflections (red). Supplementary Figure 1f shows a dark field image taken using the blue reflections identified in Figure S2e that imaged both the spherical and lath like precipitates, due to the proximity of the $L1_2$ and $D0_{22}$ reflections and the size of the objective aperture resulting in in overlap of adjacent $L1_2$ and $D0_{22}$ reflections. Interestingly, the morphology of the $D0_{22}$ laths were found to be orientated with their long axis aligned to {100}.

Supplementary Figure 2 shows a thermogravimetric analysis (TGA) curve for the Ni-Al-V alloy after and $900\,^{\circ}$C for $24\,$h and $700\,^{\circ}$C $100\,$h aging.When oxidised in synthetic air at $900\,^{\circ}$C, the oxidation scale was protective in nature. This is evidenced from the parabolic oxidation kinetics observed in the thermogravimetric signal. When the signal was fit with a power law ($y = x^n$), the fit yielded an exponent of n=0.52 (using the least-squares method), which is close to the theoretical value of 0.5 for parabolic kinetics. The corresponding oxidation rate constant was 0.63 mg^2/cm^4 hr, which was larger than that for IN718 at the same temperature, where Greene and Frinock [23] reported rate constants in the range 0.01-0.02 mg^2/cm^4 hr.
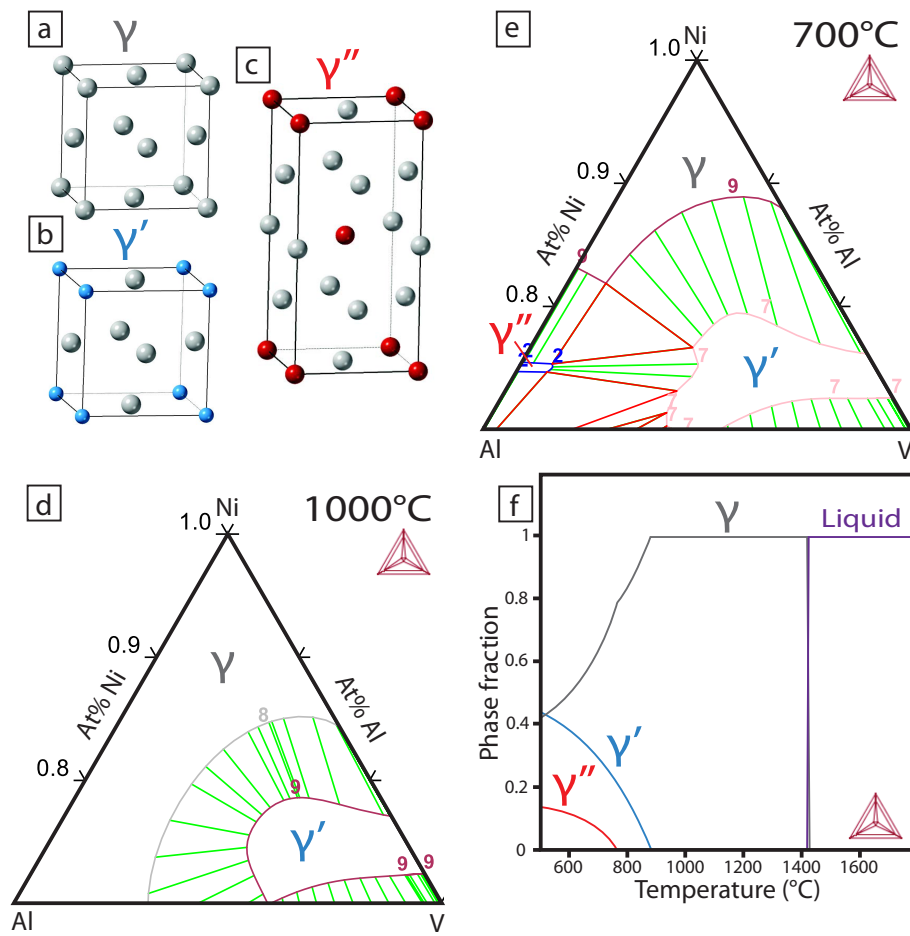
Figure 1: Unit cells of: (a) A1 fcc γ, (b) L1$_2$ ordered-fcc γ', (c) D0$_{22}$ ordered-fcc γ''. Al-Ni-V phase diagram isothermal sections predicted by Thermo-Calc TCNi8 at: (d) 1000 °C, (e) 700 °C. (f) Ni-14.9%V-5.2%Al (at.%) alloy predicted phase fractions vs temperature.
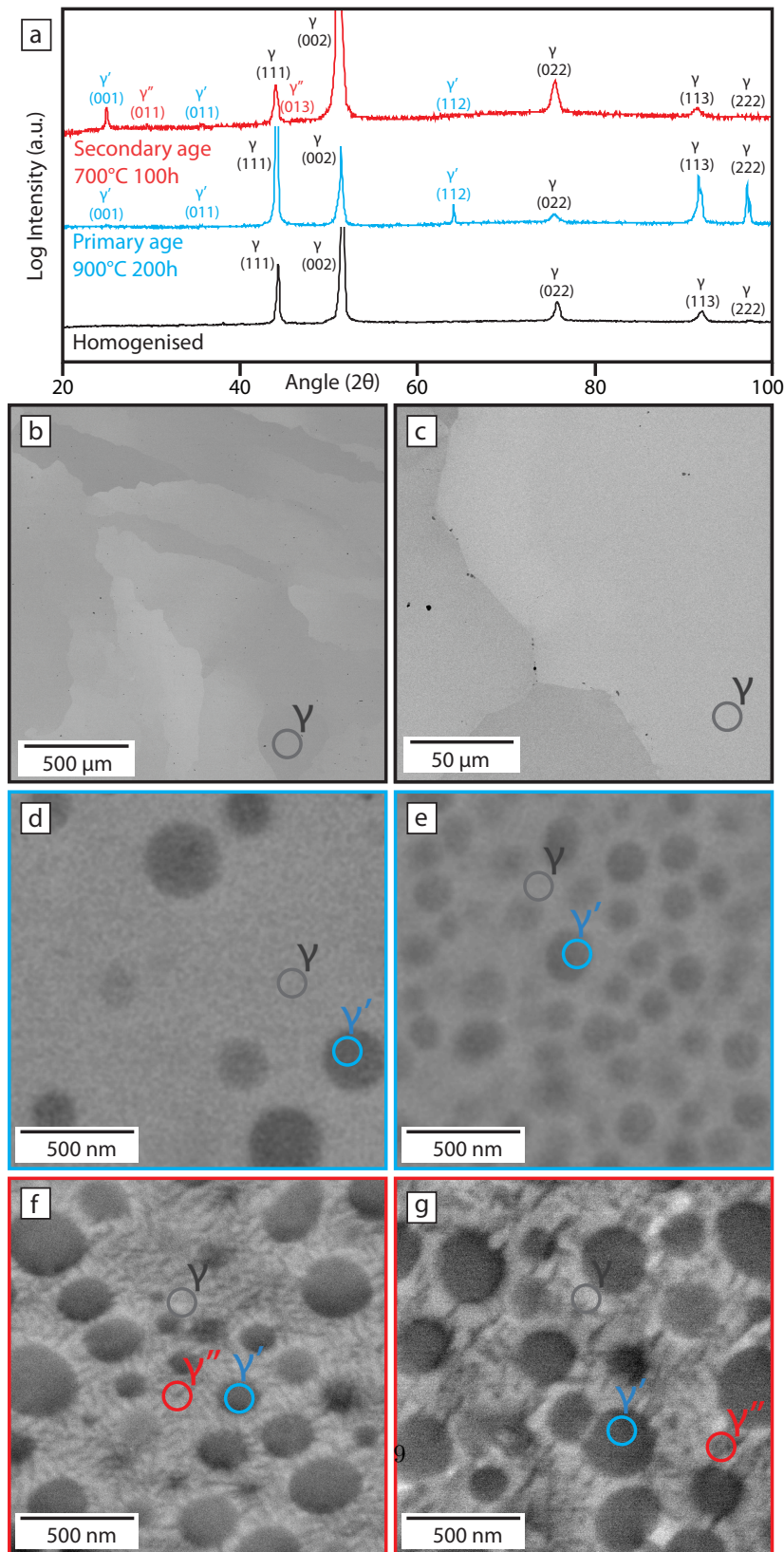
Figure 2: Ni-V-Al alloy (a) X-ray diffraction patterns, as well as backscattered SEM micrographs of (b) as-cast, (c) homogenised at 1240 °C for 24 h, (d) primary aged at 1000 °C for 16 h, (e) primary aged at 900 °C for 200 h followed by a secondary age at 700 °C for (f) 100 h and (g) 1000 h.
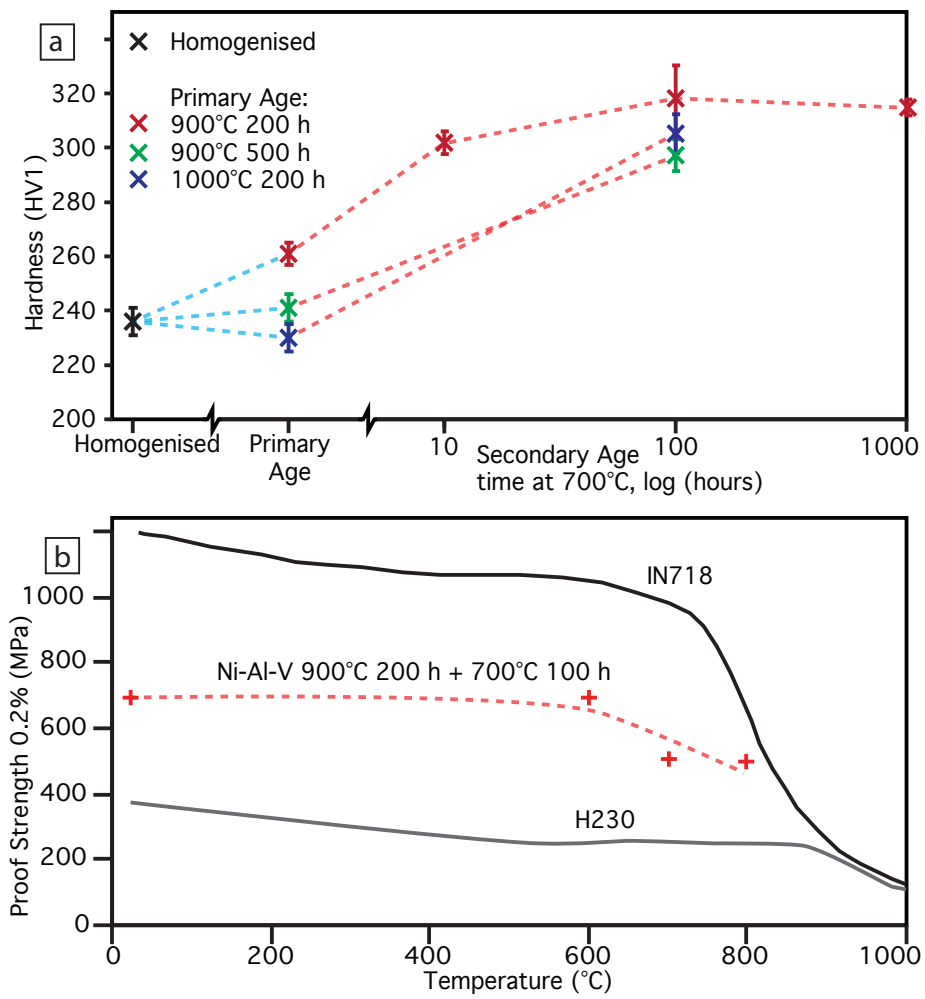
Figure 3: Ni-Al-V alloys (a) Hardness value for the respective heat treatments and ageing curve at 700 °C, (b) 0.2% compressive proof stress plotted against IN718 and H230 tensile proof strengths, adapted from [3] and [22] respectively.
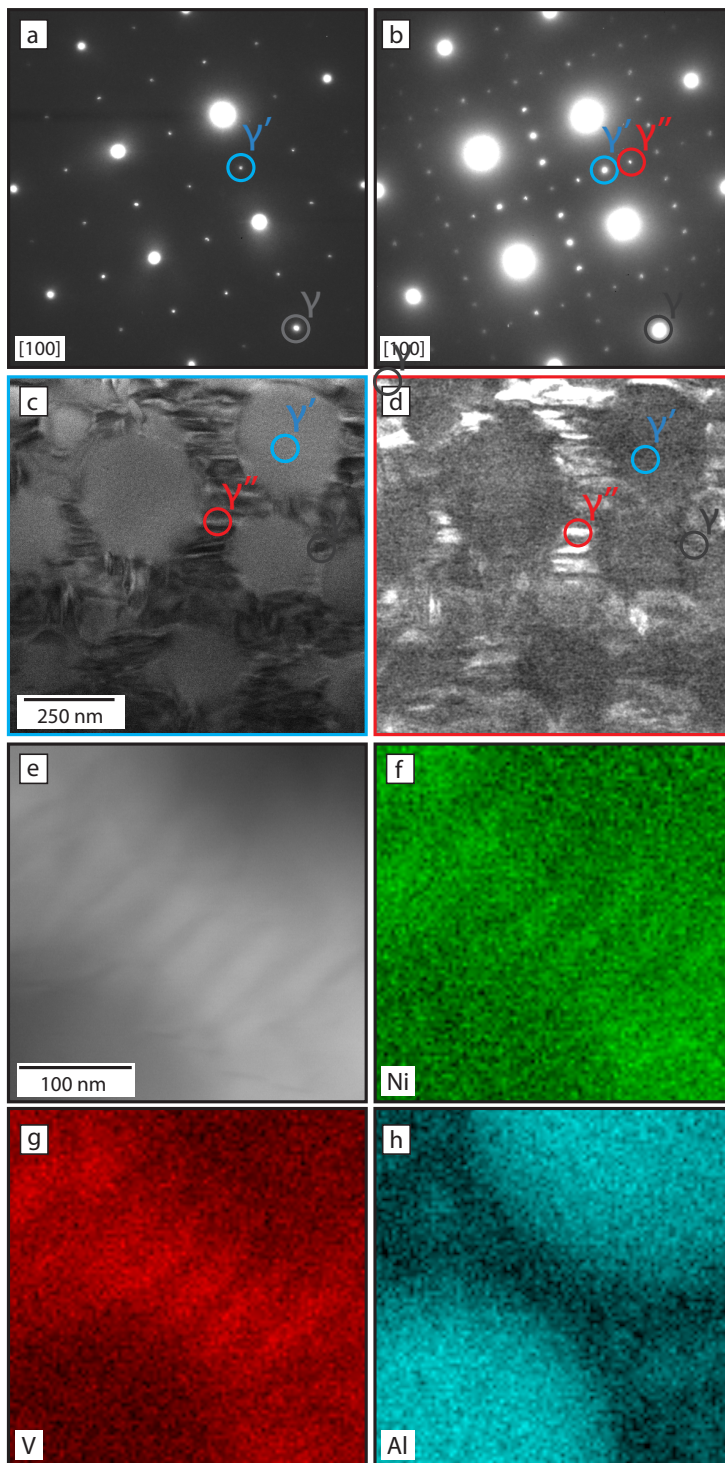
Figure 4: Alloy following secondary ageing at 700 °C for 1000 h: (a) SAPD from a spherical L1$_2$ Ni$_3$Al precipitate, (b) SAPD from matrix and both spherical and lath precipitates, (c) STEM-ADF with aperture around blue circled reflection, (d) STEM-ADF with aperture around red circled reflection. (e) STEM-HAADF, with STEM-EDX maps for (f) Ni, (g) V and (h) Al.
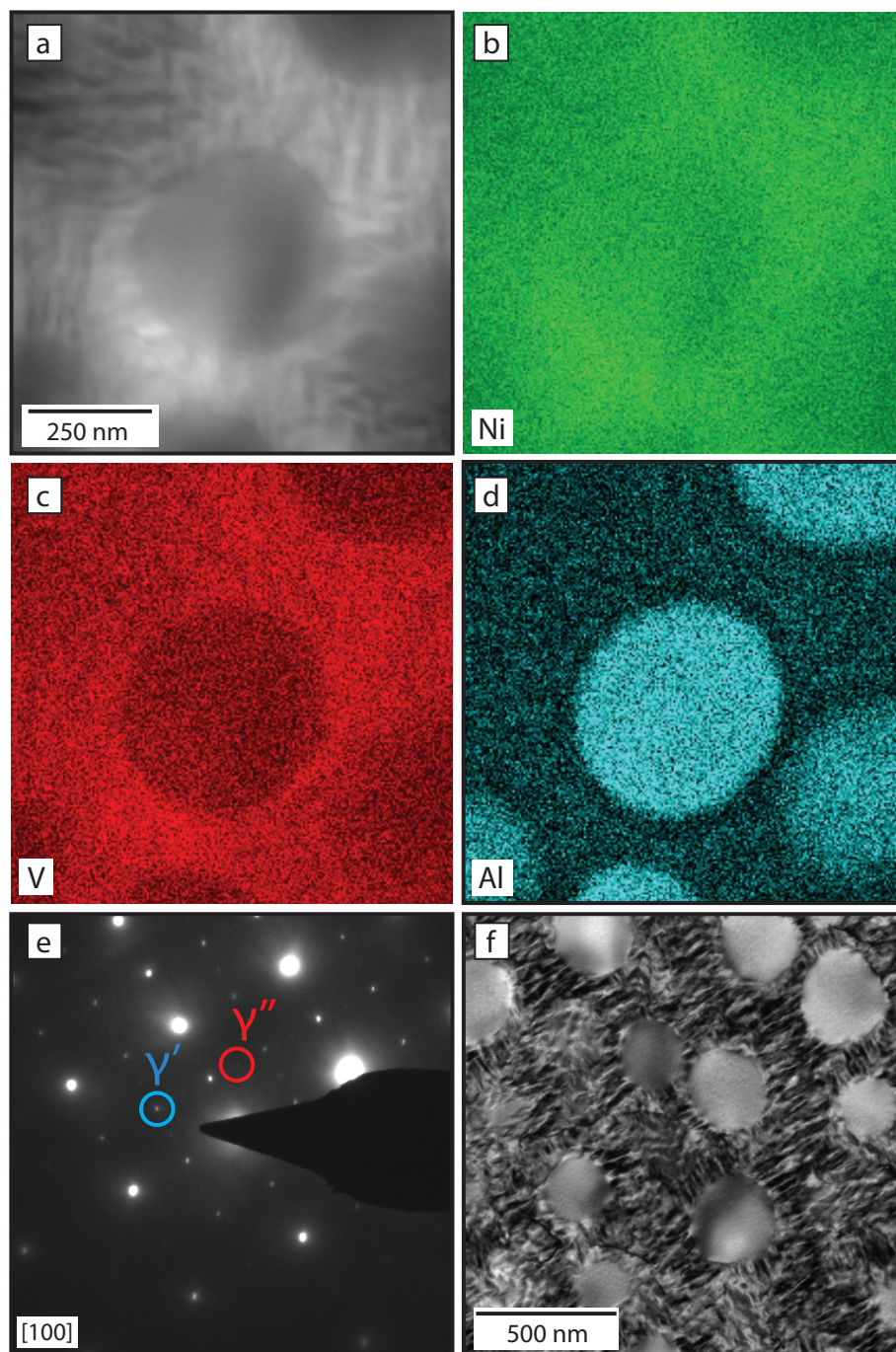
Figure S1: Alloy following secondary ageing at $700\,^\circ$C for $100\,$h: STEM (a) HAADF, with corresponding elemental maps for (b) Ni, (c) V and (d) Al, as well as (e) SADP including A1, L1$_2$ (blue) and D0$_{22}$ reflections, with (f) a dark field micrograph taken using reflection highlighted in blue on (e).
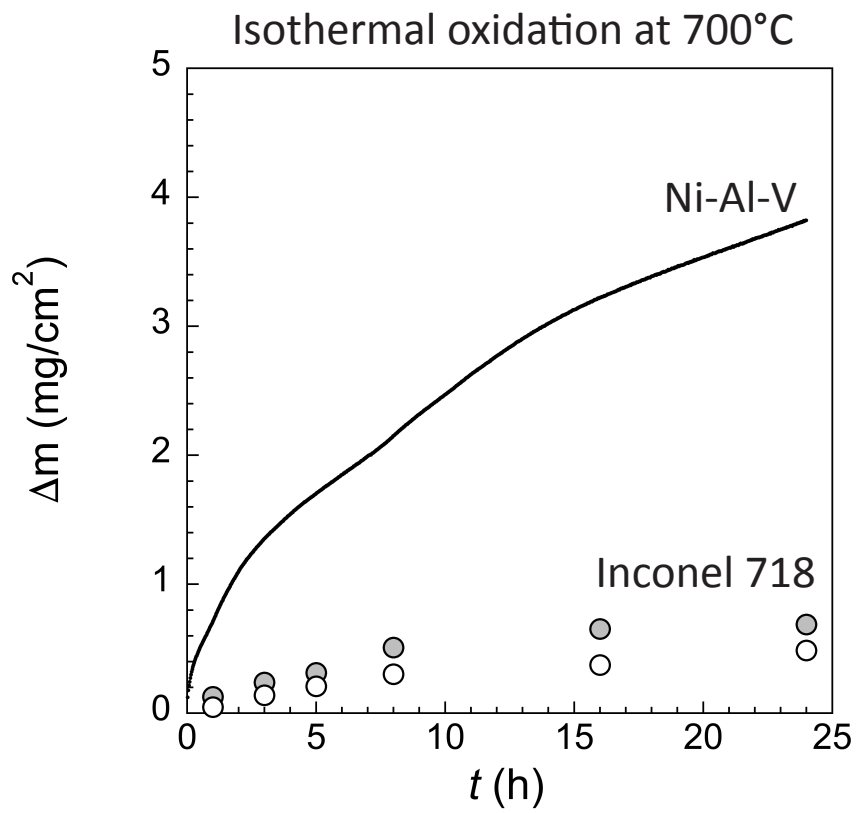
Figure S2: TGA curve for the Ni-Al-V alloy following secondary ageing at $700\,^\circ$C for $100\,$h, with data for IN718 minimum and maximum mass gain per unit area adapted from [23].